ADVANCED FUNCTIONAL MATERIALS
www.afm-journal.de

Tunable Hierarchical Metallic-Glass Nanostructures

Sundeep Mukherjee, Ryan C. Sekol, Marcelo Carmo, Eric I. Altman, André D. Taylor, and Jan Schroers*

Synthesizing metallic nanostructures with control over morphology, surface chemistry, and length-scale is important for a wide range of applications. Nanostructures having large surface area paired with suitable chemistry are particularly desirable in catalytic applications to facilitate the reaction kinetics. However, the techniques used for nanostructure synthesis are often lengthy, difficult, require expensive precursors/stabilizers, and limit the control over nanostructure morphology/chemistry. Here tuning metallic-glass nanostructures to a wide range of morphologies, where the surface is enriched with catalytic noble metal, is reported. By combining thermoplastic nanofabrication together with electrochemical processing, hierarchical metallic nanostructures with large electrochemical surface area and high catalytic activity are synthesized. Due to the versatility in processing and independent control over multiple length-scales, the approach may serve as a tool-box for fabricating complex hierarchical nanostructures for wide ranging applications.

1. Introduction

Materials for catalytic applications require large electrochemical surface area combined with desirable chemistry to facilitate reaction kinetics. Noble metal nanoparticles such as platinum/palladium make up the majority of catalyst materials, especially for fuel cell applications, because of their high activity for hydrogen/alcohol oxidation and oxygen reduction.[1,2] However, the poor durability and dispersion of the supported nanoparticle catalysts continues to be a major road-block in their performance. Shape control[3–5] and alloying[6–8] in nanostructures have been demonstrated to enhance electrocatalytic activity. But the nanostructure synthesis routes offer limited control over morphology and length-scale.[9–11] Accelerated development of potent, low-cost electrocatalysts requires efficient synthesis of hierarchical nanostructures with morphologies that provide high dispersion and effective utilization of the active noble metal.

Metallic-glasses are potential candidates for electrocatalytic applications due to their favorable chemical composition[12] and unique ability for thermoplastic manipulation at the nanometer length-scale.[13] They are multicomponent metallic alloys that exist in a wide range of chemical compositions, including catalytic noble metals such as platinum and palladium.[14–17] Due to their amorphous nature, metallic glasses are homogeneous and isotropic down to the sub-nanometer scale. Here, we report on electrochemically tuning the surface of $Ni_{60}Pd_{20}P_{17}B_3$ metallic glass from a nanoporous structure to a highly anisotropic dendritic morphology. We demonstrate that by starting with a homogeneous and isotropic amorphous surface, the chemistry and morphology can be tuned to obtain hierarchical nanostructures with high catalytic activity. Since the amorphous structure does not have any intrinsic size limitation, they can be tuned at the atomic length-scale.

2. Results and Discussion

Figure 1 shows the electrochemical processing routes in an acidic medium used to obtain nanostructures with large electrochemical surface area from $Ni_{60}Pd_{20}P_{17}B_3$ metallic glass (preparation and characterization of the amorphous alloy is described in the Experimental Section), where the surface is enriched with catalytically active palladium. Depending on the range of applied potential, very different structures form. For potentials in the shaded region (between E_{C1} and E_{C2}) in Figure 1a, an open-cell nanoporous structure is obtained. The mechanism for morphology evolution in this potential range is shown schematically in Figure 1b and the resulting nanostructure in Figure 1c. For potentials less than E_{C1}, the surface of the alloy is passivated and remains planar. Above E_{C2}, there is non-selective dissolution of all the elements from the alloy.

Between E_{C1} and E_{C2}, there is selective dealloying (Figure 1b) wherein the less-noble atoms in the alloy (Ni, P, and B) dissolve, leaving behind the more-noble palladium atoms on the surface.[18] Enhanced surface diffusion of the palladium atoms at the alloy-electrolyte interface results in Pd-clusters, which eventually grow into a nanoporous network. As seen

S. Mukherjee,[+] J. Schroers
Department of Mechanical Engineering and Materials Science
Yale University
New Haven, CT 06511, USA
E-mail: sundeep.mukherjee@unt.edu
S. Mukherjee, R. C. Sekol, M. Carmo, E. I. Altman, A. D. Taylor, J. Schroers
Center for Research on Interface Structures and Phenomena (CRISP)
Yale University
New Haven, CT 06520, USA
R. C. Sekol, M. Carmo, E. I. Altman, A. D. Taylor
Department of Chemical and Environmental Engineering
Yale University
New Haven, CT 06511, USA
[+] Present address: Department of Materials Science and Engineering, University of North Texas, Denton, TX 76203, USA

DOI: 10.1002/adfm.201202887

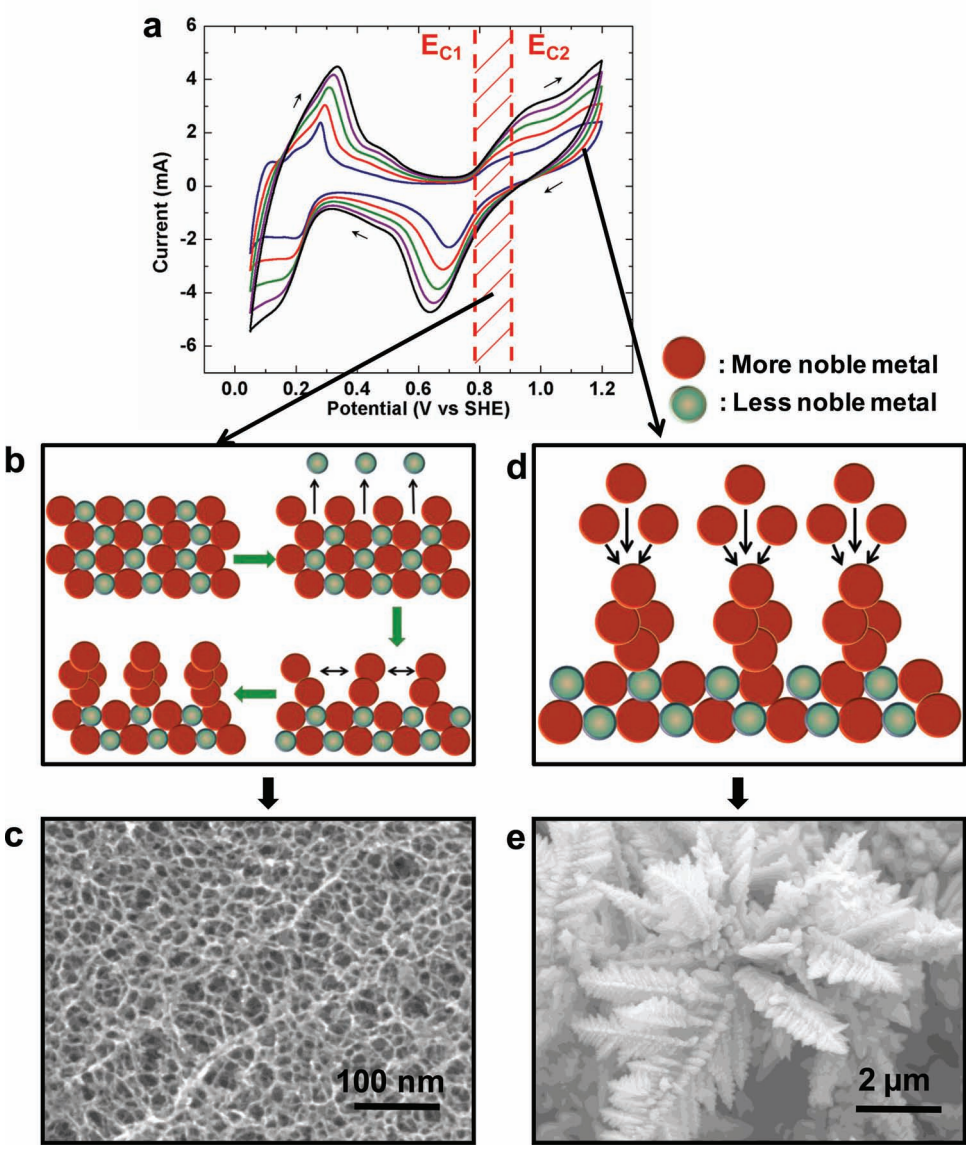

Figure 1. Electrochemically tuning the morphology of $Ni_{60}Pd_{20}P_{17}B_3$ metallic-glass nanostructures. a) Electrochemical processing routes used to obtain $Ni_{60}Pd_{20}P_{17}B_3$ metallic glass nanostructures in 0.5 mol L^{-1} H_2SO_4 solution. Up on applying a constant voltage in the shaded region between E_{C1} (≈0.8 V vs. SHE) and E_{C2} (≈0.9 V vs. SHE), a nanoporous structure is obtained. Cyclic potential sweeps (direction of sweep is shown by the short black arrows) in the range of 0.05 V–1.20 V (vs. SHE) results in highly branched dendritic structures. b) Schematic representation of selective dealloying at a potential between E_{C1} and E_{C2}, where-in the less noble atoms (blue) are removed, leaving behind the more noble atoms (red) on the surface. Surface diffusion of the more noble atoms results in clustering and growth of nanoporous network. c) SEM image of open-cell nanoporous structure obtained by selective de-alloying of $Ni_{60}Pd_{20}P_{17}B_3$ metallic glass. d) Re-deposition of more-noble atoms (red) during reverse sweep of cyclic voltammetry (schematic) results in dendritic structures. e) SEM image of highly branched dendritic nanostructures obtained by cyclic voltammetry on the surface of $Ni_{60}Pd_{20}P_{17}B_3$ metallic glass.

in Figure 1c, nanoscale porosity is obtained with pore sizes in the range of 10 to 30 nm. The porous network is comprised of very fine ligaments, less than 5 nm in diameter. Recently, electrochemical dealloying has been utilized to achieve nanoporous structures in other metallic-glasses.[19,20] The lack of grain boundaries in the amorphous alloy results in a very uniform nanostructure up on dealloying. This is in contrast to crystalline alloys, which are susceptible to preferential chemical attack along the high-energy interfaces between crystal grains typically resulting in a coarser, non-uniform nanostructure.[21,22]

Cyclic potential sweeps to a value above E_{C2} results in dissolution and re-deposition of palladium atoms (Figure 1a). Highly branched dendrites with nanoscale sub-structures were obtained by this processing route. The mechanism for dendrite formation is schematically shown in Figure 1d and the resulting nanostructure in Figure 1e. In the voltage range of 0.9 V–1.2 V (vs. standard hydrogen electrode (SHE)), electrochemical oxidation of Pd results in a surface layer of poorly soluble palladium oxide as shown by the characteristic Pd-oxidation peak in Figure 1a.[23,24] During the reverse sweep, this

oxide layer on the surface undergoes reduction to deposit pure Pd.[23,24] Energy dispersive X-ray (EDX) spectroscopy shows that the dendrites are almost pure palladium (>98 at% Pd). Oriented attachment of the Pd atoms leads to branching and growth of these anisotropic nanostructures.[25,26] Cyclic potential sweeps on a pure-metal flat surface results in roughness and faceting.[24,27] However, the $Ni_{60}Pd_{20}P_{17}B_3$ metallic glass surface acts as a self-assembling template (Figure 1d) during cyclic voltammetry, resulting in growth of highly anisotropic metallic dendrites. Thus, large surface area metal nanostructures are obtained without the need for expensive templates, precursors, or surfactants.

In standard supported catalysts, the nanoparticles detach from carbon support, resulting in significant loss of catalytic activity over time.[28] In contrast, one-dimensional nanorod structures show much better durability and dispersion of the active metal.[12,29,30] The unique thermoplastic processing ability of metallic glasses allows easy and scalable fabrication of amorphous nanorods.[13] **Figure 2**a shows scanning electron microscope (SEM) image of 200 nanometer diameter $Ni_{60}Pd_{20}P_{17}B_3$ metallic glass nanorods with an aspect ratio of five. These structures were fabricated through thermoplastic forming, which is based on the unique softening of the metallic glass when heated above its glass transition temperature (further details about the thermoplastic forming of $Ni_{60}Pd_{20}P_{17}B_3$ metallic glass are given in the Experimental Section). High yield of nanorods is obtained in less than a minute of processing time. A high-resolution transmission electron microscope (TEM) image of one such nanorod is shown in Figure 2b and the corresponding elemental line-scan is shown

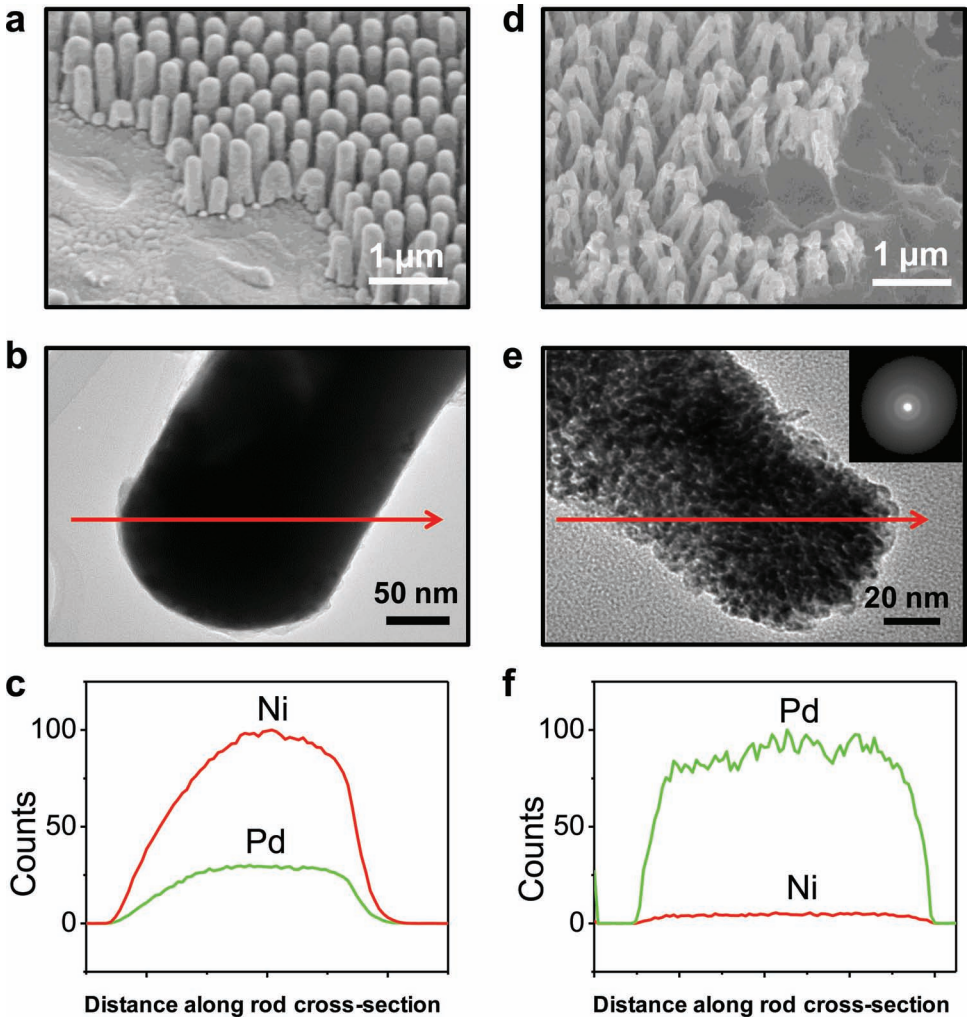

Figure 2. Thermoplastic forming and electrochemical dealloying of $Ni_{60}Pd_{20}P_{17}B_3$ nanorods. a) SEM image of 200 nm diameter $Ni_{60}Pd_{20}P_{17}B_3$ metallic glass nanorods obtained by thermoplastic forming at 390 °C and an applied pressure of about 100 MPa in alumina mold. b) TEM image of a single 200 nm diameter as-formed $Ni_{60}Pd_{20}P_{17}B_3$ nanorod with the red arrow showing the direction of composition line-scan. c) Line-scan profile of Ni and Pd along the red arrow for the nanorod shown in (b). d) SEM image of nanoporous Pd-rich nanorods obtained after dealloying for 25 min. Significant shrinkage in rod diameter is seen due to selective removal of the less-noble components of the alloy. e) TEM image of a dealloyed nanorod with the red arrow showing the direction of composition line-scan. The inset shows the associated selected area electron diffraction (SAED). The continuous diffused ring instead of dotted pattern suggests grain-size of the order of a few nanometers. f) Line-scan profile of Ni and Pd for the dealloyed nanorod showing that the nanoporous skeleton primarily consists of palladium.

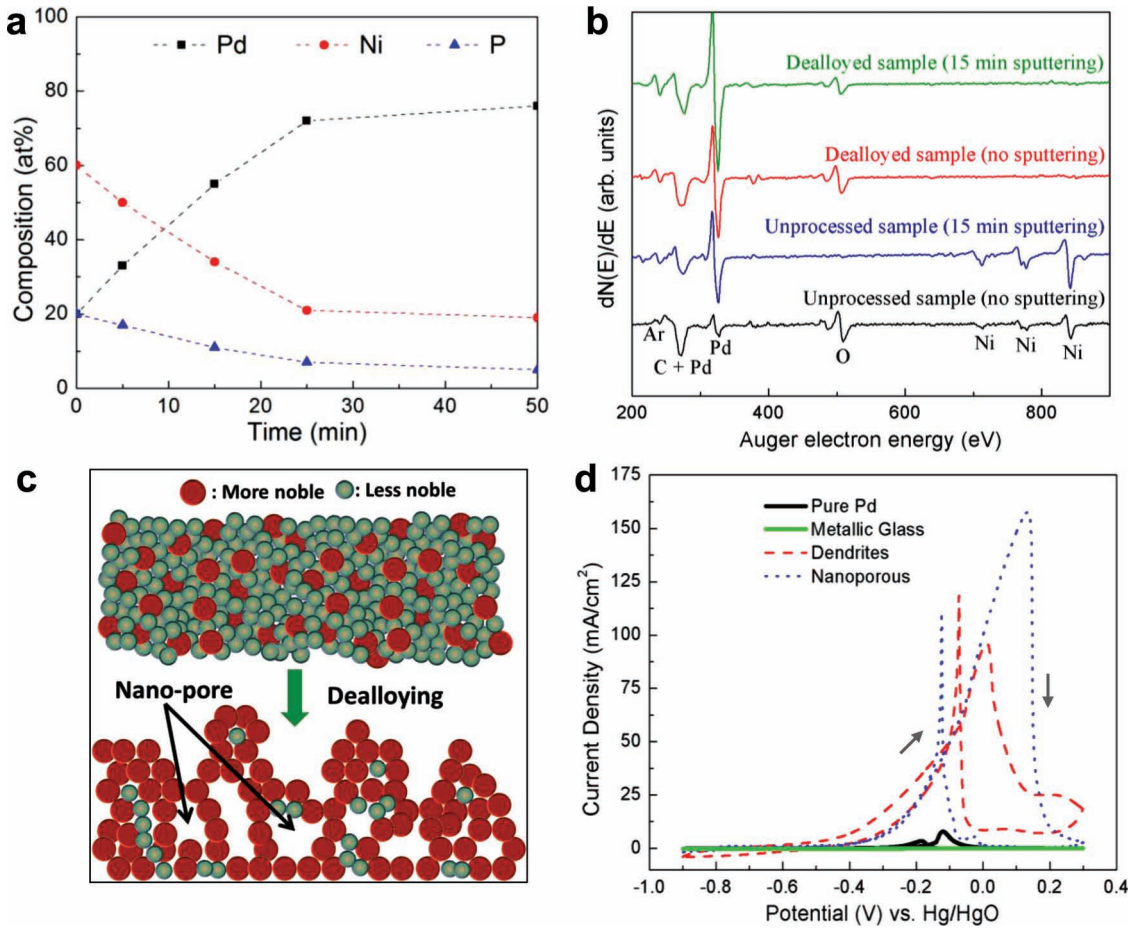

Figure 3. Composition evolution and electrocatalytic properties of nanostructures obtained from $Ni_{60}Pd_{20}P_{17}B_3$ metallic-glass. a) Rate of dealloying studied by EDX spectroscopy on an amorphous $Ni_{60}Pd_{20}P_{17}B_3$ alloy surface. Starting with 20/60 at% Pd/Ni in the amorphous alloy, the composition approaches 80/20 at% Pd/Ni after 50 min of dealloying. The trace amount of boron in the alloy could not be detected by EDX. Error in composition measurement is estimated to be within ±3%. The solid symbols represent the actual measured data points, while the connecting lines help in reading the trend. b) Surface atomic layer composition studied by AES. The dealloyed surface shows negligible nickel peaks (< 2 at% Ni) indicating that the surface is almost entirely composed of palladium atoms with traces of carbon/oxygen impurities. c) Schematic distribution of atoms before and after dealloying. The unprocessed amorphous alloy has random distribution of atoms and is single phase. After dealloying, the less noble atoms (blue) are removed from the surface leaving the more noble atoms (red) as the catalytically active shell in the nanoporous network. d) Electrocatalytic activity of nanostructures obtained from $Ni_{60}Pd_{20}P_{17}B_3$ metallic glass for methanol oxidation (scan rate of 20 mV/s). 1.0 mol L^{-1} methanol in 1.0 mol L^{-1} KOH solution was used as the electrolyte. Direction of voltage sweep is shown by the short black arrows. The starting $Ni_{60}Pd_{20}P_{17}B_3$ amorphous alloy surface shows negligible activity (green solid line). The nanoporous surface and the palladium-rich dendrites show an order of magnitude higher activity and lower onset potential for methanol oxidation compared to pure-palladium, which is attributed to their unique morphologies and chemistry induced changes in their electronic structure.

in Figure 2c. The relative distribution of Ni and Pd is uniform across the nanorod cross-section with no apparent elemental segregation (Figure 2c).

To enrich the surface of the nanorods with catalytically active palladium, they were dealloyed in the potential range between E_{C1} and E_{C2}. The surface of the nanorod becomes porous, with significant shrinkage in rod diameter (Figure 2d). The high-resolution TEM image of a dealloyed nanorod (Figure 2e) shows surface pore diameters on the order of 10 nm. The selected area electron diffraction (SAED) pattern in the inset of Figure 2e shows a diffused halo around the central bright spot, indicating a fine-grain structure of the dealloyed nanorod (the order of a few nanometers). The corresponding composition scan (Figure 2f) indicates that almost all the nickel from the alloy is selectively removed, leaving behind a nanoporous palladium-rich nanorod.

To determine the rate of selective dealloying, EDX spectroscopy was carried out on a $Ni_{60}Pd_{20}P_{17}B_3$ metallic glass flat surface with increasing dealloying time (**Figure 3**a). Starting with 1:3 Pd:Ni in the $Ni_{60}Pd_{20}P_{17}B_3$ amorphous alloy, the average composition approaches 4:1 Pd:Ni after 50 minutes of dealloying. There is no significant change in composition with further dealloying, indicating saturation of surface enrichment within the sampling depth of EDX (of the order of a few micronmeters). The surface atomic layers of the dealloyed nanostructure were studied by Auger electron spectroscopy (AES)

(Figure 3b). The unprocessed amorphous alloy surface shows peaks corresponding to Ni, Pd, and impurities such as carbon/oxygen. Once the contamination layer is removed, the ratio of Ni to Pd remains unchanged as the surface is argon ion sputtered. This suggests that there is no elemental segregation in the starting unprocessed alloy. In contrast, the AES spectrum after dealloying shows negligible nickel peaks (<2 at% Ni), indicating that the surface is almost entirely composed of palladium atoms with traces of carbon/oxygen surface impurities. The distribution of atoms in the unprocessed alloy and that obtained after dealloying is shown schematically in Figure 3c. The starting amorphous alloy is single-phase with random distribution of atoms and dealloying results in a large surface area nanoporous network. The ligaments in the nanoporous structure are composed almost entirely of palladium atoms on the surface with some residual nickel atoms in the core (Figure 3b).

In order to characterize the electrocatalytic activity of the different nanostructures, cyclic voltammetry for methanol (CH_3OH) oxidation was carried out in an alkaline medium (Figure 3d). 1.0 mol L^{-1} KOH solution with 1 mol L^{-1} CH_3OH was used as the electrolyte and potentials were determined using mercury-mercury oxide (Hg/HgO) as the reference electrode. The current density obtained for the nanoporous structure is compared with that of the dendritic nanostructure, pure-Pd surface, and the starting unprocessed amorphous alloy (Figure 3d). Each surface shows two distinct peaks: the forward peak attributed to methanol oxidation and the reverse peak associated with the removal of incompletely oxidized species.[31] The starting $Ni_{60}Pd_{20}P_{17}B_3$ amorphous alloy surface shows negligible activity.

Both the nanoporous surface and the dendritic structure show over an order of magnitude higher peak current density compared to pure-Pd surface (Figure 3d). In addition to the higher current densities, both the nanostructures show lower onset potential (≈200 mV) compared to pure-Pd surface. The high catalytic activity of the nanoporous surface is further confirmed by the higher forward peak compared to the reverse peak (Figure 3d), suggesting lesser accumulation of poisoning intermediates.[31] On the other hand, the dendritic morphology is likely to be susceptible to poisoning effects as seen from the similar peak currents in forward and reverse scans. The nanoporous morphology, together with the synergistic influence of the alloying elements in the core, promotes effective electrooxidation of methanol.[8,32] This demonstrates that chemistry induced changes in surface electronic structure are important in developing new catalysts in addition to complex morphologies with large electrochemical surface area.

3. Conclusions

Our nanostructure synthesis method represents a versatile toolbox for fabrication of a wide range of morphologies and length-scales with tailored properties by combining thermoplastic forming together with electrochemical processing. In addition to the large surface area, enrichment with respect to the active noble metal results in favorable electronic structure for electrocatalysis. The hierarchical nanostructures provide high dispersion of the catalytic metal and are self-supporting, eliminating the need for carbon-support that is commonly used in fuel cells. The control over length-scale, morphology, and electronic structure can be enhanced by using the starting composition as an additional processing parameter to realize the requirements for a wide range of electrocatalytic applications.

4. Experimental Section

Amorphous alloy with nominal composition of $Ni_{60}Pd_{20}P_{17}B_3$ was prepared in vacuum-sealed silica tubes by melting high-purity nickel, palladium, phosphorus, and boron. Fully amorphous rods were achieved by water quenching molten samples from a temperature of 1000 °C after appropriate B_2O_3 fluxing. X-ray diffraction (XRD) of a section of $Ni_{60}Pd_{20}P_{17}B_3$ rod displayed a broad diffraction maximum with no observable crystalline peaks, confirming the amorphous nature of the alloy.

$Ni_{60}Pd_{20}P_{17}B_3$ amorphous alloy was thermoplastically processed in the super-cooled liquid region above its glass transition temperature. The metallic glass softened into a viscous liquid at the thermoplastic forming temperature and flowed into the mold pattern under a controlled applied pressure. Commercially available anodized alumina molds were used as a template for the nanoforming. Based on the crystallization and viscosity data of the $Ni_{60}Pd_{20}P_{17}B_3$ metallic glass, the forming of 200 nanometer diameter nanorods was done at a temperature of 390 °C under an applied pressure of about 100 MPa. The metallic glass nanorods were released from the alumina molds by etching with KOH solution.

For cyclic voltammetry (CV), $Ni_{60}Pd_{20}P_{17}B_3$ metallic glass was used in a classical three-electrode setup. The amorphous alloy was incorporated as the working electrode into a rotating-disk electrode setup from PINE Instruments. Potentials were determined using a SHE as the reference electrode in acidic medium and Hg/HgO in alkaline medium.

Acknowledgements

This work was primarily supported by the National Science Foundation under MRSEC DMR-1119826.

Received: October 4, 2012
Revised: December 5, 2012
Published online: January 14, 2013

[1] B. C. H. Steele, A. Heinzel, *Nature* **2001**, *414*, 345.
[2] A. D. Taylor, M. Michel, R. C. Sekol, J. M. Kizuka, N. A. Kotov, L. T. Thompson, *Adv. Funct. Mater.* **2008**, *18*, 3003.
[3] N. Tian, Z.-Y. Zhou, S.-G. Sun, Y. Ding, Z. L. Wang, *Science* **2007**, *316*, 732.
[4] J. Zhang, H. Yang, J. Fang, S. Zou, *Nano Lett.* **2011**, *10*, 638.
[5] Y. Xia, Y. Xiong, B. Lim, S. E. Skrabalak, *Angew. Chem. Int. Ed.* **2009**, *48*, 60.
[6] V. R. Stamenkovic, B. S. Mun, M. Arenz, K. J. J. Mayrhofer, C. A. Lucas, G. Wang, P. N. Ross, N. M. Markovic, *Nat. Mater.* **2007**, *6*, 241.
[7] M.-H. Shao, K. Sasaki, R. R. Adzic, *J. Am. Chem. Soc.* **2006**, *128*, 3526.
[8] S. Koh, P. Strasser, *J. Am. Chem. Soc.* **2007**, *129*, 12624.
[9] Y. Xiong, J. Chen, B. Wiley, Y. Xia, S. Aloni, Y. Yin, *J. Am. Chem. Soc.* **2005**, *127*, 7332.
[10] J. P. Xiao, Y. Xie, R. Tang, M. Chen, X. B. Tian, *Adv. Mater.* **2001**, *13*, 1887.

[11] S. Porel, N. Hebalkar, B. Sreedhar, T. P. Radhakrishnan, *Adv. Funct. Mater.* **2007**, *17*, 2550.
[12] M. Carmo, R. C. Sekol, S. Ding, G. Kumar, J. Schroers, A. D. Taylor, *ACS Nano* **2011**, *5*, 2979.
[13] G. Kumar, H. X. Tang, J. Schroers, *Nature* **2009**, *457*, 868.
[14] A. L. Greer, *Science* **1995**, *267*, 1947.
[15] W. L. Johnson, *MRS Bull.* **1999**, *24*, 42.
[16] A. Inoue, *Acta Mater.* **2000**, *48*, 279.
[17] J. Schroers, *Adv. Mater.* **2010**, *22*, 1566.
[18] J. Erlebacher, M. J. Aziz, A. Karma, N. Dimitrov, K. Sieradzki, *Nature* **2001**, *410*, 450.
[19] J. Yu, Y. Ding, C. Xu, A. Inoue, T. Sakurai, M. Chen, *Chem. Mater.* **2008**, *20*, 4548.
[20] L. Battezzati, F. Scaglione, *J. Alloys Compd.* **2011**, *509*, *Supplement 1*, S8.
[21] R. Morrish, K. Dorame, A. J. Muscat, *Scr. Mater.* **2011**, *64*, 856.
[22] X. Lu, T. J. Balk, R. Spolenak, E. Arzt, *Thin Solid Films* **2007**, *515*, 7122.
[23] K. Juodkazis, J. Juodkazyte, B. Sebeka, G. Stalnionis, A. Lukinskas, *Russ. J. Electrochem.* **2003**, *39*, 954.
[24] C. L. Perdriel, E. Custidiano, A. J. Arvia, *J. Electroanal. Chem. Interfacial Electrochem.* **1988**, *246*, 165.
[25] R. L. Penn, J. F. Banfield, *Science* **1998**, *281*, 969.
[26] J. Watt, S. Cheong, M. F. Toney, B. Ingham, J. Cookson, P. T. Bishop, R. D. Tilley, *ACS Nano* **2010**, *4*, 396.
[27] J. Gomez, L. Vazquez, A. M. Baro, N. Garcia, C. L. Perdriel, W. E. Triaca, A. J. Arvia, *Nature* **1986**, *323*, 612.
[28] P. J. Ferreira, G. J. la O', Y. Shao-Horn, D. Morgan, R. Makharia, S. Kocha, H. A. Gasteiger, *J. Electrochem. Soc.* **2005**, *152*, A2256.
[29] C. W. Xu, H. Wang, P. K. Shen, S. P. Jiang, *Adv. Mater.* **2007**, *19*, 4256.
[30] C. Pan, H. Wu, C. Wang, B. Wang, L. Zhang, Z. Cheng, P. Hu, W. Pan, Z. Zhou, X. Yang, J. Zhu, *Adv. Mater.* **2008**, *20*, 1644.
[31] Y.-W. Lee, S.-B. Han, K.-W. Park, *Electrochem. Commun.* **2009**, *11*, 1968.
[32] J. Greeley, J. K. Nørskov, *Surf. Sci.* **2005**, *592*, 104.